Processing TiC nanoparticle reinforced aluminum matrix composites in PBF-LB: Powder blending approach, particle sintering, precipitation and grain refinement

Raphael Freundl [*], Eric A. Jägle

Institute of Materials Science, Fakultät für Luft- und Raumfahrttechnik, Universität der Bundeswehr München, Werner-Heisenberg-Weg 39, 85579 Neubiberg, Germany

ARTICLE INFO

ABSTRACT

Particle-reinforced aluminum-matrix-composites (AMCs) promise enhanced mechanical properties while maintaining the lightweight potential of aluminum. Fabricating AMCs near-net-shape is desirable because it avoids the drawback of the difficult machining. Laser powder bed fusion (PBF-LB) has the potential to achieve this goal. An economically attractive powder blending approach was used to modify AlSi7Mg0.6 powder with TiC nanoparticles. The resulting blend was processed in a PBF-LB machine to fabricate AMCs. This paper shows how to maximize the grain refinement potential of TiC nanoparticles by using a high mixing time of 1215 min to break up agglomerates. For a better understanding of the process related microstructure, investigations of the TiC distribution in blend and composites have been conducted by SEM and EDS. The formation of TiC microparticles formed by sintering of agglomerates are an integral part of the final microstructure. Measuring the overall carbon content of the specimens reveals a loss of TiC during PBF-LB. The root causes are discussed in terms of agglomeration and smoke generation and countermeasures are proposed. The presented approach is an effective way to introduce nanoparticles and to refine the microstructure. It can also be adapted to other material systems to modify the grain size and reduce the texture.

1. Introduction/motivation

Particle reinforced Metal Matrix Composites (MMCs) combine the good ductility and toughness of metals with the high modulus and hardness of ceramic particles to create superior material properties [1]. In many cases, aluminum and its alloys are used as matrix material since they offer a distinct lightweight potential due to its low density in comparison to steel [2,3].

A major drawback is the difficult machining of MMCs, that is caused by the hard ceramic particles, which are embedded in the matrix [4–6]. Therefore, a near-net-shape fabrication method is beneficial to avoid this issue [7]. One possible approach could be casting, but as the particle content increases, the viscosity of the melt increases and filigree structures are no longer feasible [8–10]. Furthermore, the solidification front velocity is often not fast enough to exceed a critical value which is necessary to prevent particle pushing, ensuring a homogeneous particle distribution [8,11]. This problem is more pronounced for nanoparticles, since the critical velocity depends on the particle size and is particularly high for small particles [12].

Another option are additive manufacturing techniques, which have gained more and more attention over the last years. The most common approach for metal additive manufacturing is Laser-Powder-Bed-Fusion (PBF-LB). In addition to the near-net-shape fabrication, this process offers another advantage, which is the rapid solidification that should alleviate or even eliminate particle pushing, leading to a homogeneous microstructure and associated properties of the composite material [8].

In recent years, the introduction of very small particles in the nanometer size range has attracted attention, particularly in the context of PBF-LB, which is the processing technique used in the current study [13–15]. These Metal Matrix Nanocomposites (MMNCs) typically contain only a small amount of ceramic particles ($\approx$ 1 vol%) [16]. Nevertheless, investigations have proved a significant increase in strength by nanoparticle addition compared to the unreinforced matrix and their microcomposite counterparts [17–23].

There exist several types of ceramic nanoparticles like TiB_2 (requires an excess of Ti in the melt to form an Al_3Ti surface layer which nucleates aluminum), Al_3Ti, AlB_2 and TiC, which is used in the present study, that are known to act as efficient inoculants in aluminum alloys and lead to a

* Corresponding author.
E-mail addresses: raphael.freundl@unibw.de (R. Freundl), eric.jaegle@unibw.de (E.A. Jägle).

refined microstructure [16,24,25]. A small grain size possesses several advantages for the processing in PBF-LB as well as the bulk properties, like a reduction in hot tearing susceptibility of the material as well as better strength and good ductility [26–28]. This enables to print even aluminum alloys that are commonly known to be poorly processible in PBF-LB due to tearing [27].

In addition to the grain refinement efficiency, TiC has the advantage of a high melting temperature of 3140 °C [2]. But also, below this temperature a disintegration of TiC in liquid aluminum (alloys) might be possible when TiC dissolves due to thermodynamic instability. According to thermodynamic simulations, TiC is the stable phase at elevated temperatures when a stochiometric composition of Ti and C is present in the Al melt [29]. Only at intermediate temperatures, Ti and C can be dissolved in liquid Al. The lower temperature limit above which TiC is stable in Al varies in the literature, as summarized by Albiter et al. [30], and ranges from 700 °C–1177 °C. Above this threshold and below its melting point, TiC is not susceptible to disintegration, neither by dissolution nor by melting. The peak temperatures expected from simulations of aluminum alloy processing in PBF-LB are well within this temperature range [13,31]. Hence, TiC is a good choice for processing in the PBF-LB route. Additionally, carbides can effectively enhance the powder bed absorptivity of materials such as aluminum alloys, which have a high reflectivity at the wavelength of conventional PBF-LB lasers ($\approx$ 1064 nm) [18,32–35]. Wang et al. [35] measured a lower porosity of AlSi7Mg specimens that contained additions of 2 wt.% of SiC nanoparticles, introduced by a planetary mill, and processed by PBF-LB. They explained their findings with the enhanced absorption measured for the powder blend with SiC. However, Al_4C_3 was formed by the reaction of SiC with Al. Therefore, the present study is trying to exploit higher thermal stability of TiC compared to SiC.

MMC powders containing TiC nanoparticles within the metal microparticles, having been introduced during atomization, are not commercially available. The molten salt approach of Lin et al. [18] for nanoparticle incorporation results in excellent mechanical properties such as high strength and specific modulus, but is very time consuming and costly. High-energy ball milling, on the other hand, carries the risk of destroying the sphericity and thus the flowability of the powder feedstock [36]. Hence, this paper investigates the applicability of a simple and economically attractive procedure to create a TiC nanoparticle-containing raw material that can be processed via the PBF-LB route.

The approach presented here is based on a blending process in a tumble mixer. The aim was to achieve a homogeneous coating of the AlSi7Mg0.6 microparticles by the TiC nanoparticles. Gärtner et al. [37] demonstrated that parameters such as mixing duration play a crucial role in achieving a homogeneous distribution of adhered nanoparticles on the surface of the microparticles. Opprecht et al. [27] showed that a uniform distribution of nanoparticles on the surface is in principle possible with this technique. In contrast to the experiments of Opprecht et al. [27], no additional mixing aids (zirconia balls) were used for the + 1 wt.% TiC containing blends in order to evaluate if it is possible to further minimize the complexity and to avoid the laborious removal of the balls after the blending process. The aim of the present study was to gain knowledge about the correlation of all steps during fabrication of nanoparticle reinforced AMCs. Beside the influence of the mixing duration on the resulting nanoparticle distribution in the blend, the effect of this distribution and the TiC content on the final microstructure was determined.

2. Methods

2.1. Blending process

To prepare the powder blend, two powders were mixed in a tumble mixer (Turbula T2F, WAB-Group) at a mixing speed of 101 min^{-1} in a glass bottle (volume of 120 ml). The matrix alloy powder was inert gas atomized, pre-alloyed AlSi7Mg0.6 (TLS Technik GmbH & Co.), with spherical particles and a particle size of 20–63 μm. Detailed composition and size distribution can be found in Table 1 and Table 2 in the appendix. The second powder was TiC nanopowder with a mean particle size of 50 nm (IoLiTec Ionic Liquids Technologies GmbH).

For two of the three composite blends used in this study, the content of TiC nanoparticles (TiCnm) added was 1 wt.% ($\approx$ 0,54 vol%), respectively. These two blends differ only in their mixing state (defined by the blending duration). The applied blending durations were 15 min and 1215 min and no mixing aids were used. The third blend contained 5 wt.% TiCnm ($\approx$ 2,70 vol%) and was blended for 135 min with 3 g mixing balls (NETZSCH ZETABEADS 3,0) to accelerate agglomeration breakup. The mixing durations are inspired by the time steps used in flowability measurement (not shown here) that were carried out to guarantee sufficient powder flowability of the blends. For the flowability measurements the blends were mixed with durations of $5*3^x$ min (integer x: $0 \leq x \leq 5$). The total weight of each blend was 60 g.

2.2. Laser additive manufacturing

Manufacturing of the MMCs was carried out using a TruPrint 1000 PBF-LB machine by Trumpf equipped with a single laser (fiber laser, 1064 nm wavelength, 200 W max. power, 32.6 μm focus diameter). The samples were cubes of 10x10x10 mm^3 for the polished cross-sectional specimens and cuboids with 3x3x5 mm^3 for the specimens used for the carbon content measurements. A parameter study was previously conducted to determine the parameters necessary to produce near full density samples for the pure matrix. These parameters include laser power, scan speed, and hatch spacing, which were 175 W, 1815 mm/s, and 90 μm, respectively. They were applied to all samples, i.e. no individual parameter optimization for the MMC feedstocks was performed. The scanning strategy was a single laser exposure (no remelting) with a simple hatching. A 45° clockwise rotation of the scan direction was applied after each layer. The layer height was 20 μm. The substrate plate was not preheated.

2.3. Analytical Methods

For the analysis of the specimens, polished cross sections were prepared along the build direction and perpendicular to the scan tracks of the top layer using standard metallographic techniques. The final step was colloidal silica polishing.

Powder size measurements were performed using a Bettersizer S3 Plus particle size and shape analyzer (3P Instruments GmbH & Co.KG). The optical analysis method using the camera has been conducted. The measurement was running for at least 10,000 counts to obtain a steady state value for D10, D50 and D90 which describe the particle size that is not exceeded by 10 %, 50 % and 90 % of the total number of particles measured. The software used was the Bettersize Analysis System V8.10.

SEM images were taken with a Zeiss Gemini Ultra 55. EDS data were acquired with an ELITE SUPER EDX detector from EDAX using an acceleration voltage of 6 kV at a working distance of 8.5 mm. We chose an acceleration voltage below the lower level of effective excitation of Ti because we also wanted to detect C and for this element we already exceed the upper value of effective excitation. So, this acceleration voltage is a compromise. Nevertheless, for all relevant elements the acceleration voltage is above the level necessary to excite Kα. Since the quantification was not the goal but rather the local distribution of the elements (mapping), 6 kV is fine. In addition, a lower acceleration voltage (compared to the effective excitation level of Ti) can help to keep the excitation volume smaller, which is beneficial for the detection of small nanoparticles as we investigate in this study. EBSD measurements were conducted with an EDAX VELOCITY PRO. The software for EDS and EBSD was EDAX APEX version 2.5.1001.0001. The EBSD images show the crystal orientation parallel to the build direction.

The carbon content was measured using a CS-Analyzer from

Elementar Analysesysteme GmbH (inductar cube CS). For the powder analyzed, large, visible TiCnm agglomerates were deliberately excluded from the measurement (by selectively picking up the powder with a spatula) to ensure that only the carbon belonging to the TiCnm adhering to the surface of the AlSi7Mg0.6 particles was measured.

3. Results

3.1. TiC particle distribution in the raw material

Fig. 1 and Fig. 2 confirm that the TiCnm used are well within a reasonable size range around the specified size of 50 nm with a limited number of particles reaching $\geq$ 100 nm. The raw TiCnm powder shows agglomerates even before the mixing process (see Fig. 1). The reason for the high tendency for clustering are the Van–der–Waals (VDW) forces that play a crucial role when dealing with nanoparticles, whose force per weight ratio is significantly higher than for micron-sized particles [14,38].

The mixing process to produce the blends leads to another kind of nanoparticle agglomerate. Fig. 2 shows one of the TiCnm agglomerates formed after a mixing duration of 15 min. These newly formed agglomerates can have a size that significantly exceeds the dimensions of the raw powder agglomerates and is comparable to the largest particles of the AlSi7Mg0.6 powder (i.e., tens of μm). They show a much more densified character, and a smother surface compared to those in the as-delivered powder. We will refer to them as "big" TiCnm agglomerates.

To evaluate whether a longer mixing duration can lead to a change in nanoparticle distribution, a second powder blend was prepared with the same composition but with an extended mixing duration of 1215 min. Fig. 3 shows macroscopic images of the two powder blends. The black areas are the big TiCnm agglomerates. It is clearly visible that a longer mixing duration can alleviate clustering. The high number of agglomerates present after 15 min mostly disappears after additional 20 h of mixing. The TiCnm agglomerates in the blends were tolerated and poured together with the rest of the blend into the powder reservoir of the PBF-LB machine before the print job.

The EDS maps in Fig. 4 confirm that the big (tens of μm) agglomerates that have formed during the first minutes of mixing have been broken up and vanished during additional mixing. Many of the nanoparticles that previously had been integrated in the big agglomerates are now, after 1215 min of mixing, on the surface of the AlSi7Mg0.6 particles. This is indicated by a higher intensity of the yellow color (Ti detection) on the AlSi7Mg0.6 particle surface (see Fig. 4) and can be verified in the SEM at higher magnification (see Fig. 5).

Some of the AlSi7Mg0.6 particles exhibit areas of increased Ti concentration (see Fig. 4, right). A closer inspection of these areas reveals a special kind of nanoparticle agglomerate, which looks like a continuous particle shell that is coating a limited area of the AlSi7Mg0.6 particle

surface (see Fig. 6). The number of these "shell" areas has increased significantly after the long mixing time (see Fig. 4). Hence, it can be concluded that the disintegration of the big nanoparticle agglomerates by prolonged mixing time is accompanied not only by a homogeneous distribution of the previously in big agglomerates bound TiCnm on the AlSi7Mg0.6 particle surface, but also by a "shell agglomerate" formation.

It can be summarized that problems associated with the formation of big agglomerates (see Fig. 2) can be overcome, but only if an adequate mixing duration is applied. In this case, additional mixing additives such as balls are not needed to break up the big agglomerates, although they can help to accelerate this process. We want to make clear that for some discussions it is necessary to distinguish between *big* agglomerates (see Fig. 2), *shell* agglomerates (see Fig. 6) and *small* agglomerates (a cluster of only a few TiCnm particles). If we use only the expression *agglomerates* without a specification all kinds of agglomerates are addressed.

3.2. PBF-LB processing

Since the applied powder layer thickness (20 μm) was relatively small compared to the AlSi7Mg0.6 powder size (20–63 μm), a change in particle size distribution during deposition was expected (limited space between recoating lip and powder bed leads to preferential pushing of large particles into the overflow collector). To verify this, the average particle size was measured and compared between the powder remaining in the powder bed after deposition and the powder pushed into the collector. For the powder on the build plate D10, D50 and D90 were 28.6 μm, 45.8 μm, and 64.9 μm, respectively, and for the powder in the collector they were 30.4 μm 50.3 μm, and 70.9 μm. The results show that bigger AlSi7Mg0.6 particles are more likely to be pushed into the collector, resulting in an increase in the average particle size.

For the blend containing a high TiCnm fraction of 5 wt.%, severe smoke generation occurred during the processing, indicating a release of nanoparticles into the atmosphere (see Fig. 7).

Fig. 8 shows examples of printed cubes for the pure matrix material AlSi7Mg0.6 and the composite AlSi7Mg0.6 + 1 wt.% TiCnm (15-min-mixed blend) composite.

3.3. Carbon content analysis

The nanoparticle content in the final MMC is determined not only by the amount of TiCnm in the powder blend, but also by the mixing duration and the TiCnm loss during the process, including powder deposition and laser exposure. A detailed explanation about the correlations is made in the discussion section. Fig. 9 shows the carbon content measured by a CS-Analyzer relative to the carbon added in the form of TiCnm. Since the big TiCnm agglomerates have been deliberately excluded, as explained in the "Analytical Methods" section, the
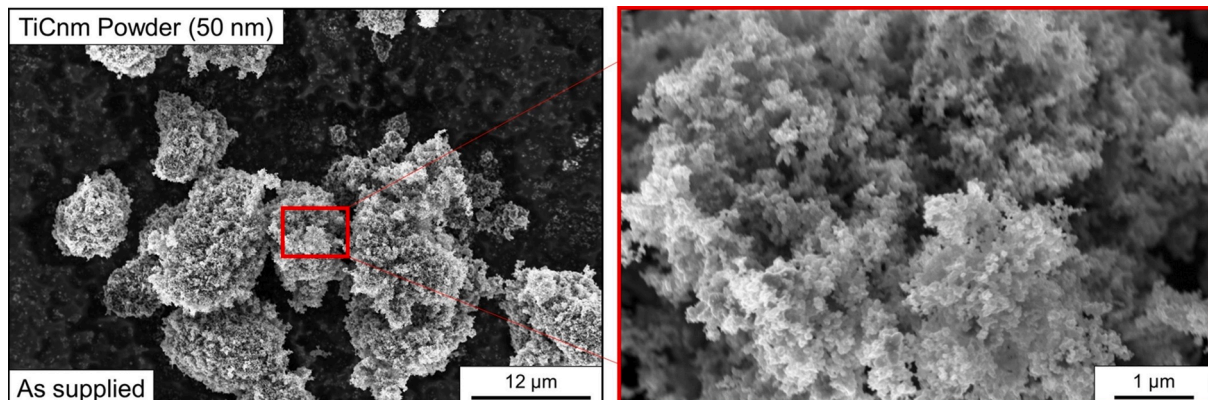

Fig. 1. As–supplied TiCnm raw powder at low magnification (left) and higher magnification (right).
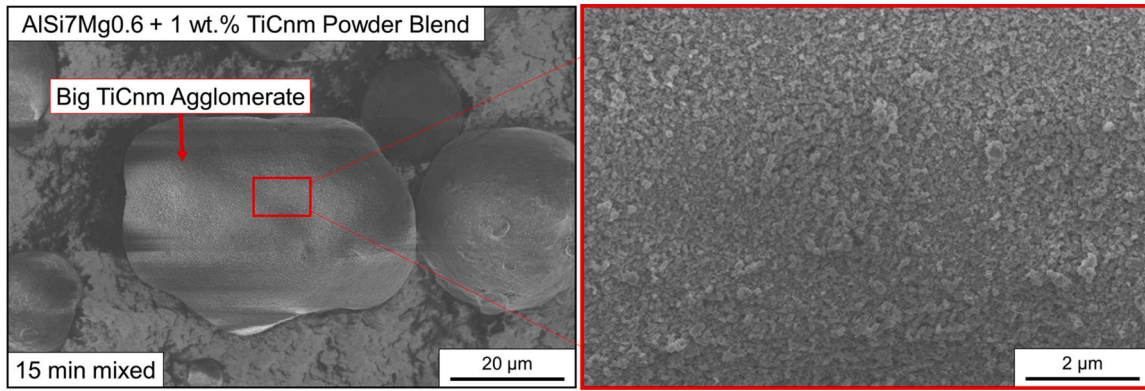
Fig. 2. Big TiCnm agglomerate after 15 min mixing duration at low magnification (left) and higher magnification (right).
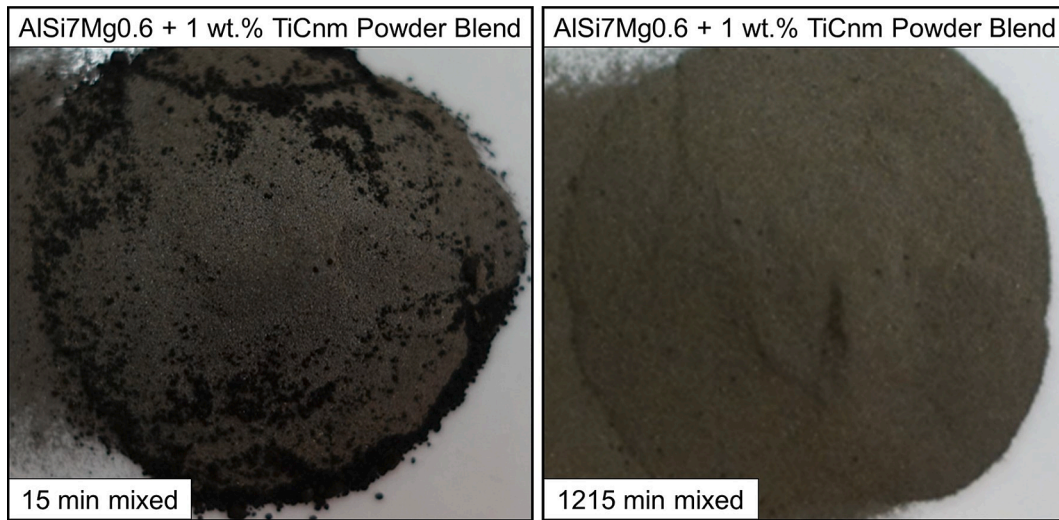

Fig. 3. Macroscopic image of powder blends after 15 min (left) and 1215 min (right) mixing duration.
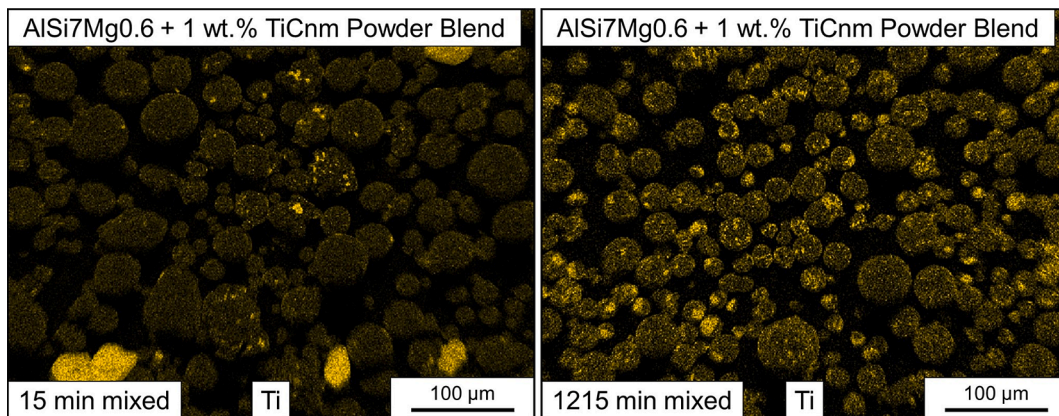

Fig. 4. EDS maps of powder blends after 15 min (left) and 1215 min (right) mixing duration. The yellow color corresponds to the detection of Ti and reveals big TiCnm agglomerates after 15 min mixing that have been broken up after 1215 min mixing duration. (For interpretation of the references to color in this figure legend, the reader is referred to the web version of this article.)

measurements give only the amount of carbon in the powder located in TiCnm which are adhesively bonded to the AlSi7Mg0.6 powder surface. Therefore, the carbon content measured for the powder is also an indication of the degree of TiCnm agglomeration. In other words, a relative C content of less than 100 % means that some TiCnm have formed big agglomerates and have been removed prior to measurement. This is most pronounced for the 15-min-mixed blend, but also the more homogeneous appearing blends (less visible big TiCnm agglomerates) experience some loss of TiCnm compared to what has been added. The laser exposure leads to a further TiCnm loss, with exception of the 1215-min-mixed blend containing 1 wt.% TiCnm.
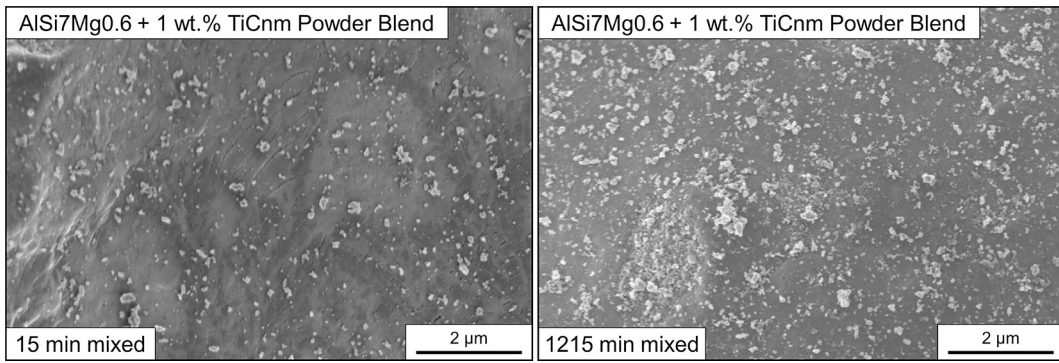
Fig. 5. TiCnm particle distribution on the AlSi7Mg0.6 particle surface after 15 min (left) and 1215 min (right) mixing duration.
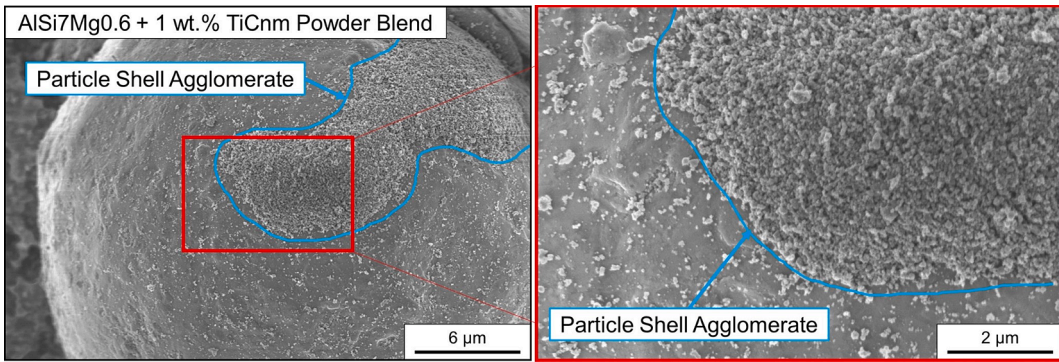

Fig. 6. During blending formed TiCnm particle shell agglomerate that partially coats the AlSi7Mg0.6 particle surface.
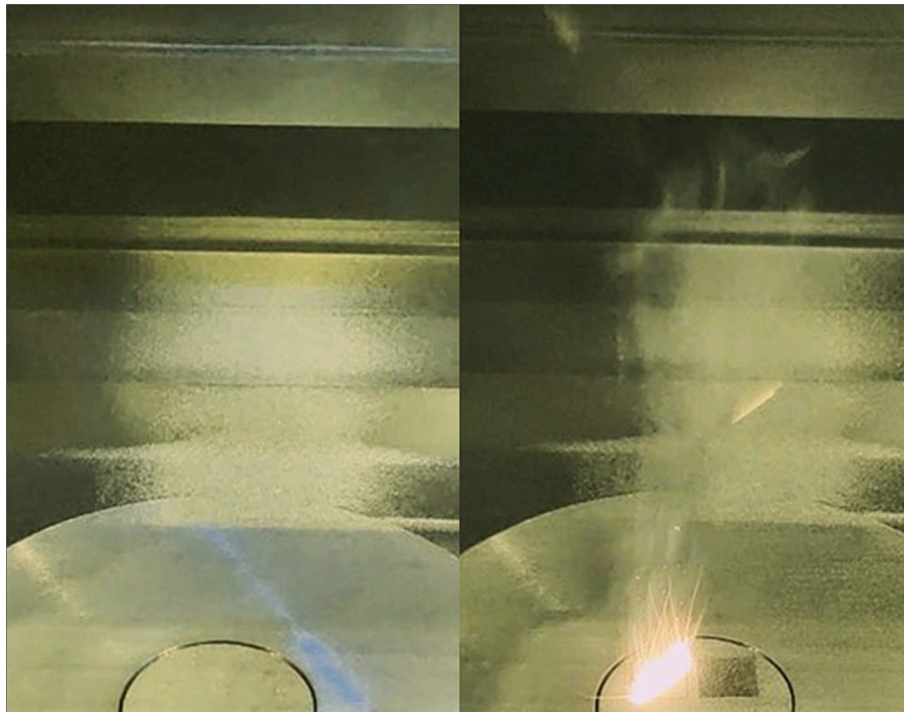

Fig. 7. Powder bed before laser exposure (left) and during laser exposure of the composite blend (AlSi7Mg0.6 + 5 wt.% TiCnm) with severe smoke generation (right).

3.4. Grain refinement

Fig. 10 (top left) shows the microstructure of the pure matrix material after PBF-LB processing. Compared to the TiC containing samples, relatively coarse columnar grains are visible. The introduction of 1 wt.% TiCnm leads to a significant grain refinement, with the grain

Fig. 8. PBF-LB fabricated $10 \times 10 \times 10$ mm^3 cubes of pure matrix material AlSi7Mg0.6 (left) and the composite AlSi7Mg0.6 + 1 wt.% TiCnm made with the 15–min–mixed blend (right).
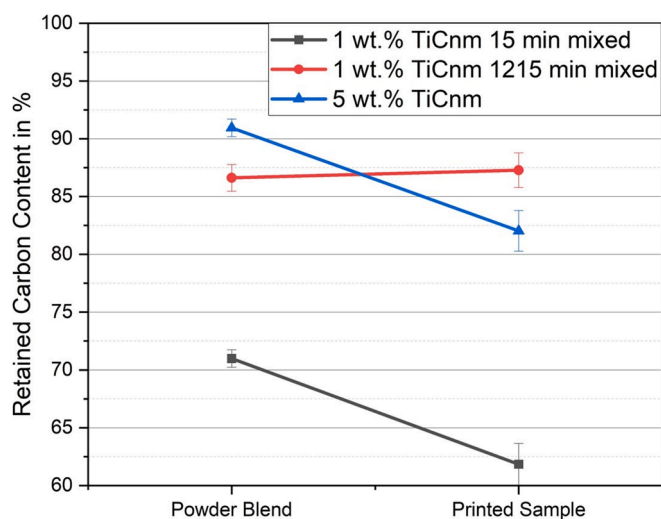

Fig. 9. Carbon content of blend and printed sample compared to carbon added in the form of TiCnm (big TiCnm agglomerates in the blend deliberately excluded).

shape changing to equiaxed. The grain refinement is more pronounced at the melt pool boundaries, but also the core of each melt pool is mostly equiaxed and significantly refined. There is a clear difference between the two MMCs made with powder blends of different mixing durations. Although both AlSi7Mg0.6 + 1 wt.% TiCnm blends feature the same nominal composition, the 1215-min-mixed blend leads to a higher TiC content in the PBF-LB-processed material (see Fig. 9), resulting in a higher degree of grain refinement. Increasing the TiCnm content to 5 wt. % leads to a fully grain refined, and mostly homogeneous microstructure. A higher magnification EBSD image of this sample is provided in the appendix (see Fig. 17).

3.5. Sintering of nanoparticle agglomerates

Fig. 11 displays three former TiCnm agglomerates in adjacent areas embedded in a solidified AlSi7Mg0.6 matrix. The matrix shows dark appearing Al cells that are surrounded by bright Si cell boundaries. This cell structure is well known for AlSi alloys fabricated in PBF-LB. Bright particles with a high Ti content precipitated and are particularly visible on the right side of the image. They seem to have an increased tendency to be located at the Si cell boundaries. These features will be discussed in

more detail in later sections.

Fig. 11 (middle particle) shows evidence that nanoparticle agglomerates are not breaking up during PBF-LB processing. Apparently, the melt pool dynamics, including the Marangoni flow, are insufficient to separate the nanoparticles contained in TiCnm agglomerates. Hence, to achieve a homogeneous distribution of nanoparticles in PBF-LB-produced material, it is necessary to distribute the TiCnm particles well in the powder blend prior to additive manufacturing.

Closer inspection of the agglomerates after PBF-LB (Fig. 12) reveals that the individual nanoparticles have fused together, presumably due to sintering, i.e., a solid-state process. The root cause for sintering is the reduction of surface energy which is particularly high for the TiCnm due to their high surface to volume ratio. Particles in two stages of sintering during laser irradiance are visible in Fig. 12. First, the individual nanoparticles form necks and sinter to form submicron-sized particles of 200 nm - 600 nm. These submicron-sized particles in turn sinter on a larger length scale until a fairly but not fully dense and solid TiC microparticle is formed that can no longer be described as nanoparticle agglomerate. We will call these newly formed TiC particles "nanoparticle originating" (NPO) TiC (micro-)particles in the following to emphasize their origin. The NPO TiC microparticles in Fig. 11 have different sinter states which also define the residual porosity. Two of them show a well sintered structure. The third in the middle reveals almost no sintering and contains the TiCnm mostly in their original size. It offers a lower density compared to the well sintered NPO TiC microparticles. Since the reduction of surface energy is the driving force for sintering, a higher degree of sintering correlates with less porosity.

3.6. Nanoparticle distribution in the composite

Low magnification light microscope images (see Fig. 13) of the cross sections reveal a homogeneous distribution of NPO TiC microparticles in the PBF-LB-processed specimens, proving that the NPO TiC microparticles do not tend to agglomerate and that the melt-flow is beneficial and does not push the NPO TiC microparticles into a certain region, such as the melt pool boundaries or center.

Fig. 14 shows an EDS mapping including a NPO TiC microparticle (lower right corner of the top images) and the local vicinity. As mentioned above, it is clear that the NPO TiC microparticle has not decomposed. In addition, several small (<100 nm) Ti-rich areas can be detected, however, there is no corresponding carbon enrichment, as would be expected for TiCnm. Instead, a closer inspection (Fig. 14, bottom images) indicates a correlation between these Ti-rich areas and an increased Si concentration.

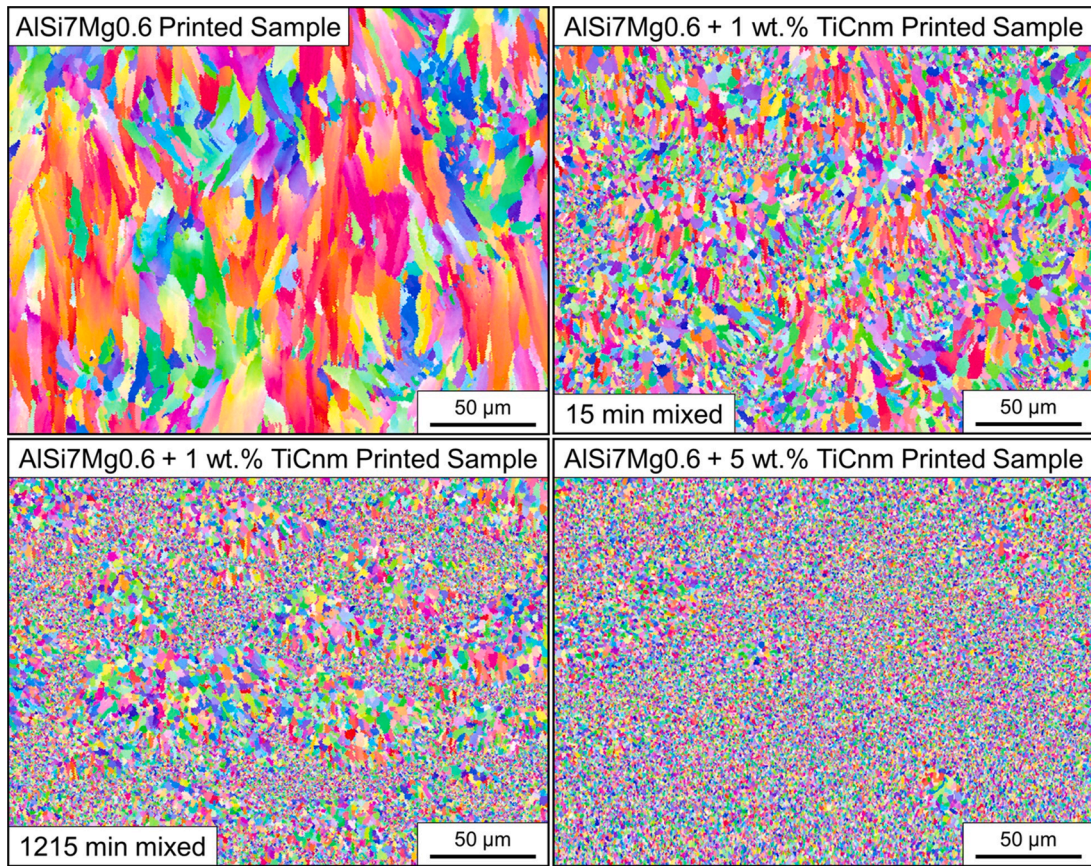Fig. 15 depicts ESB images (right) that were captured at the melt pool

Fig. 10. Grain structure of the pure matrix (top left), the composites with 1 wt.% TiCnm made from 15–min–mixed blend (top right) and 1215-min-mixed blend (bottom left) and the composite with 5 wt.% TiCnm (bottom right).
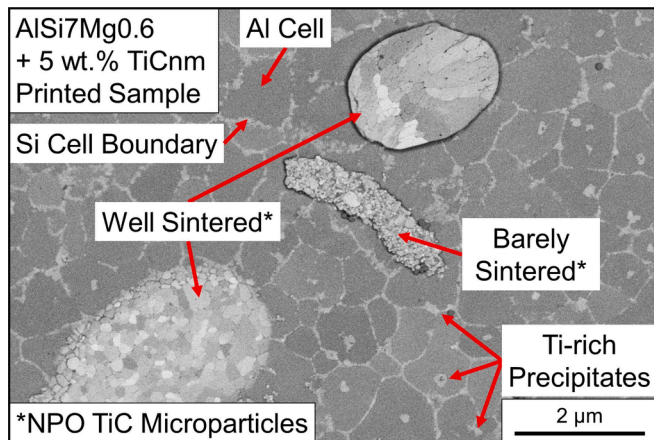

Fig. 11. ESB image of AlSi7Mg0.6 matrix consisting of Al cells surrounded by Si cell boundaries with embedded Ti-rich precipitates and NPO TiC microparticles in different sinter states: Well Sintered (top, bottom), Barely Sintered (middle) (AlSi7Mg0,6 + 5 wt.% TiCnm).

Fig. 12. Two states of NPO TiC microparticle formation with State I: sintering of the original TiCnm to submicron–sized particles and State II: sintering of the formed submicron–sized particles to a fairly dense TiC microparticle.

boundary and center of a melt pool (AlSi7Mg0.6 + 1 wt.% TiCnm made from the blend mixed for 1215 min). The results verify a high density of Ti-rich precipitates at the melt pool boundaries, however, they are nearly (but not fully) absent in the region of the melt pool center.

To better understand whether the Ti-rich particles in the matrix are unagglomerated TiCnm which have survived the PBF-LB process or newly formed precipitates, an EDS line scan crossing several of the Ti-rich areas has been conducted on the 1 wt.% TiCnm (1215-min-mixed) specimen. Fig. 16 shows the results which indicate that the Ti-
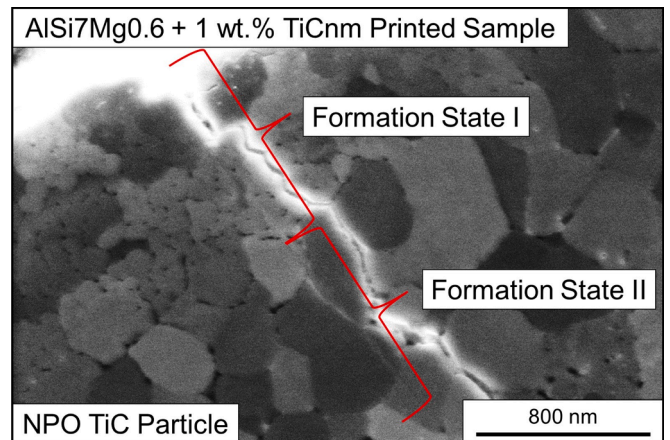
rich areas are no longer TiC particles since there is no spatial correspondence between carbon and Ti. This implies that the Ti-rich particles have been newly formed in the process by precipitation. Similarly, there is no simultaneous Ti and O enrichment, which eliminates the possibility that the particles are titanium oxide. As indicated already by Fig. 14, every Ti peak in the line scan is aligned with an increased Si content. The largest Si peaks belong to the Si cell boundaries where many of the Ti-rich precipitates are located.
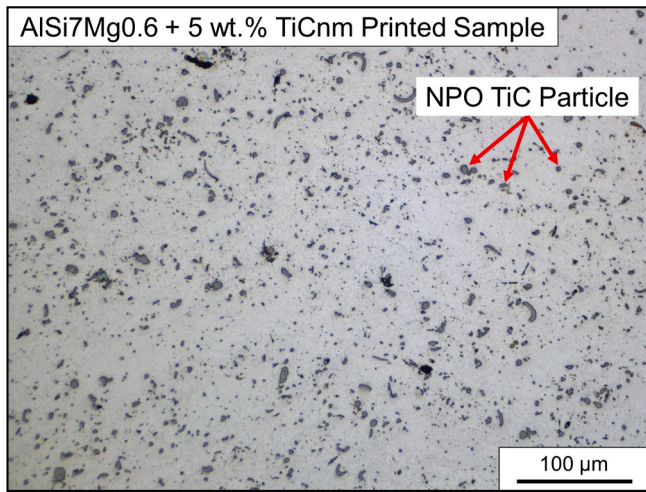
Fig. 13. Light microscope image of a polished cross section of the composite sample containing 5 wt.% TiCnm particles indicating a homogeneous NPO TiC microparticle distribution.

4. Discussion

4.1. Process induced TiC removal mechanisms

The mixing duration has a crucial influence on how the TiCnm are distributed in the final blend. A high mixing duration of 1215 min can effectively break up big TiCnm agglomerates which form during the initial steps of the blending process. The addition of mixing aids (balls)

can also help to break up big TiCnm agglomerates which allows to reduce the required mixing duration as was the case for the 5 wt.% TiCnm blend mixed for 135 min with 3 g of mixing balls. The TiCnm are then deposited on the surface of the AlSi7Mg0.6 powder particles (see Fig. 3, Fig. 4 and Fig. 5). This deposited TiC is firmly bound to the AlSi7Mg0.6 powder and is thus transferred to the PBF-LB machine when the powder blend is poured into the powder reservoir. Subsequently, it is incorporated into the final composite. Despite proper mixing, however, a certain number of TiCnm remain on the inner surface of the mixing bottle after the powder blend is poured into the PBF-LB machine. This effect explains the reduced C content in the powder blend, even for blends where the big TiCnm agglomerates are mostly broken up (see Fig. 9). The impact of this powder transfer artefact diminishes as the added TiCnm content increases, resulting in a higher proportion of retained C for the 5 wt.% powder blend. Hence, the size of the mixing vessel and the fill level are particularly relevant for small weight fractions of nanoparticles, as they define the ratio of the inner surface area of the vessel to the number of incorporated nanoparticles. Larger vessels with higher fill levels should mitigate this effect, however, this will change the mixing conditions and the occurring forces during the blending process, which will require an adjustment in the mixing durations.

Because the big TiCnm agglomerates were deliberately excluded from the powder blend measurements with the CS-Analyzer, the blend with 1 wt.% TiCnm, which was only mixed for 15 min, shows the highest carbon loss (which is a direct measure for the TiC content) of the powder blends tested. We opted to exclude the big agglomerates from the C content measurements since this imitates what is happening during the powder deposition in the PBF-LB process: Many of the big TiCnm agglomerates (up to 60 μm in size) are pushed towards the collector by the
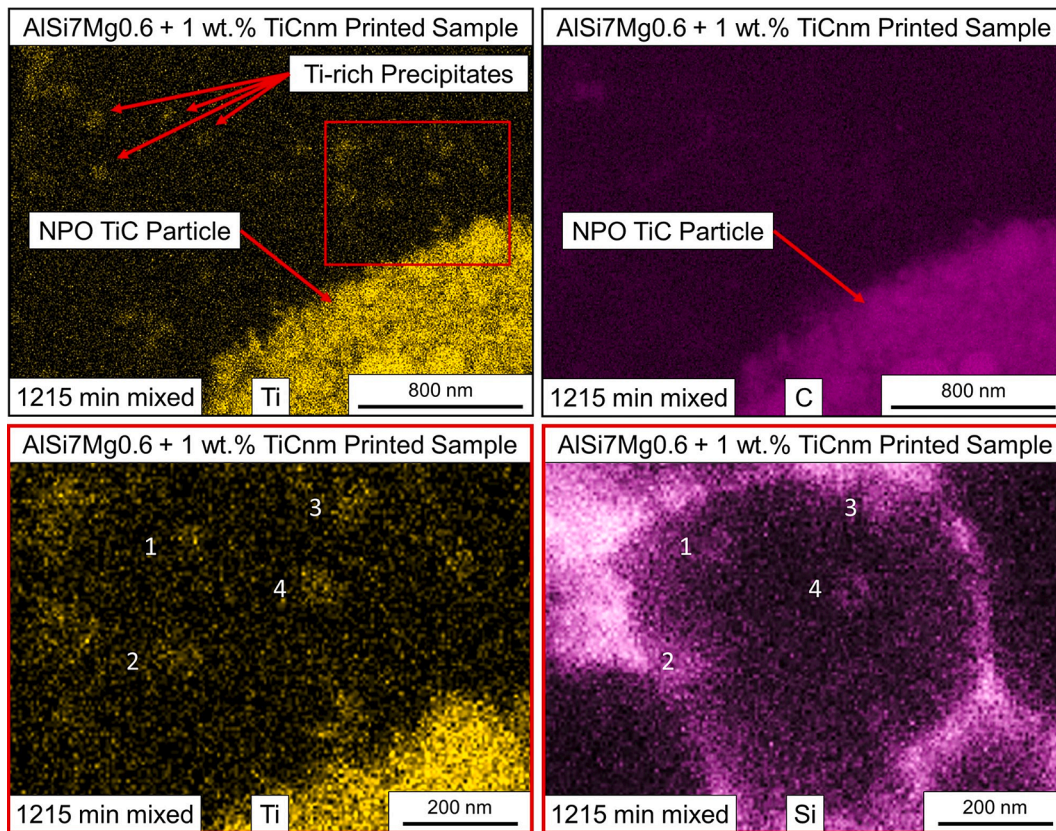
Fig. 14. EDS detection of Ti (top left), C (top right) nearby a NPO TiC microparticle indicating a disintegration of separated TiCnm particles with subsequent precipitation of Ti-rich precipitates without C and proving the stability of NPO TiC microparticles during PBF-LB process. Higher magnified area (red rectangle) with detection of Ti (bottom left) and Si (bottom right) indicating a certain degree of Si incorporation in the Ti-rich precipitates. (For interpretation of the references to color in this figure legend, the reader is referred to the web version of this article.)

Fig. 15. Optical microscope image (left) showing the investigated melt pool and the regions at the melt pool boundary and center that were used for closer examination in the SEM (right). The corresponding ESB images show a high density of Ti-rich precipitates at the melt pool boundary (bottom right), which are almost absent in the melt pool center region (top right).
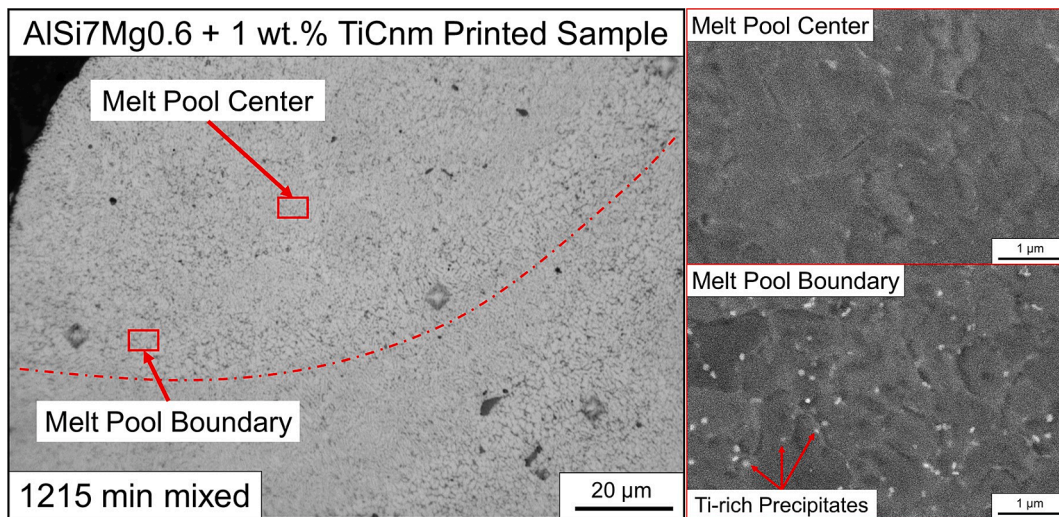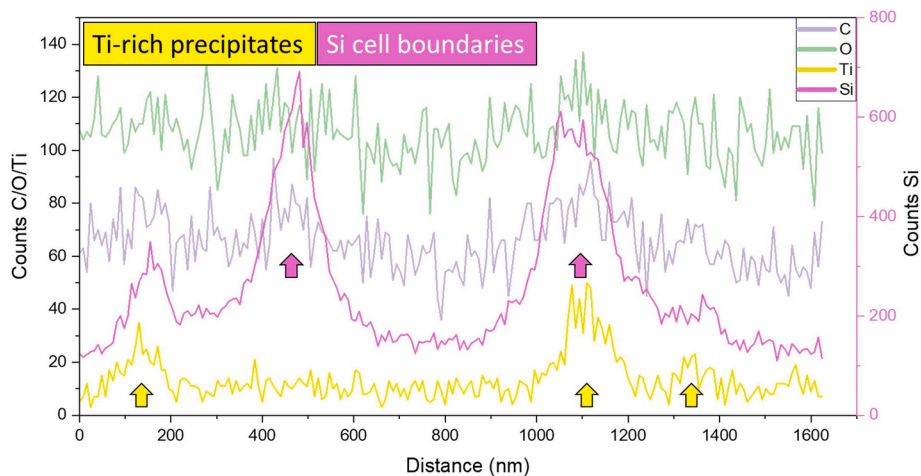

Fig. 16. EDS line scan on AlSi7Mg0.6 + 1 wt.% TiCnm (1215-min-mixed) composite crossing Ti-rich precipitates. The lack of spatial correspondence of Ti peaks with C and O indicates that Ti-rich precipitates are no TiC or titanium-oxide. The overlap with Si is due to the high probability of Ti-rich precipitates sitting on the Si cell boundaries and probably to the incorporation of a certain degree of Si into the Ti-rich precipitates.

powder recoater (powder overflow) since they significantly exceed the set layer height of 20 μm. This behavior of sorting out the bigger particles during the powder deposition has been verified by particle size measurements for the AlSi7Mg0.6 powder and is transferable to the big TiCnm agglomerates which are in the size range of the biggest AlSi7Mg0.6 particles. These TiCnm, that are integrated in the big agglomerates, are not incorporated in the final composite, leading to the lowest C content in the printed samples using this (15-min-mixed) powder feedstock. Note, however, that approach to exclude the big TiCnm agglomerates in the CS-Analyzer powder measurements may not have been completely effective. Therefore, the reported C content for the powder of the 15-min-mixed blend may be slightly overestimated as compared to the printed part.

During printing, another effect takes place that leads to a further reduction of TiCnm. This was observed to a high degree for the 5 wt.% TiCnm sample and is called "smoke" generation (see Fig. 7). It can be assumed that turbulences in the process atmosphere, which are caused by heating and evaporation of elements such as Mg leads to forces strong enough to remove the adhesively bonded TiCnm from the surface of the AlSi7Mg0.6 particles. For stable processing, it is crucial to ensure an

adequate protective gas flow speed to prevent contamination of the laser window. Due to this behavior, a significant amount of TiC gets lost during the laser exposure, leading to a reduced content in the final part. For low TiCnm contents, the influence is less pronounced (compare in Fig. 9: 1 wt.% TiCnm 1215-min-mixed with 5 wt.% TiCnm). For the 1 wt.% TiCnm 1215-min-mixed blend, there even seems to be a slight increase in C. A possible explanation could be found in the fact, that particle size sorting is also present for the TiCnm coated AlSi7Mg0.6 particles. Some of the AlSi7Mg0.6 particles are too big to remain on the baseplate and are pushed into the powder overflow. Hence, during powder deposition, the relative number of smaller AlSi7Mg0.6 particles on the baseplate increases. This in turn improves the mean surface to volume ratio of the AlSi7Mg0.6 powder. Assuming a homogeneous TiCnm density per surface area in the blend, this will cause an increased TiCnm content in the deposited powder.

4.2. Behavior of nanoparticle agglomerates in the melt pool

The behavior of TiC in Al alloys has been studied for conventional stir casting and melt infiltration [30,39]. The available literature dealing

with TiC reinforced aluminum matrix composites processed in PBF-LB is sparse and focuses on parameter optimization and mechanical properties, but can't explain the microstructural features (pronounced grain refinement at the melt pool boundaries, NPO TiC microparticles, Ti-rich precipitates) and TiC behavior (sintering, partial disintegration) in the present study [18,40–43]. In contrast to the blending approach used in this work these studies used high-energy ball milling or in case of Lin et al. [18] a pre-alloyed composite powder where the TiC was already introduced into the aluminum alloy powder particles. Furthermore, they didn't use AlSi7Mg0.6 as the matrix alloy but pure Al, AlSi10Mg or Al–Si–Mg–Ti.

In the final microstructure of the composites fabricated in this study many NPO TiC microparticles are present. They have developed from TiCnm agglomerates, indicating that these nanoparticles, which are already agglomerated prior to processing, are not breaking up in the melt pool. The stability of the nanoparticle agglomerates depends on the forces present. There are four main forces on and between nanoparticles in the melt pool: gravity, melt flow, VDW attraction, and electrostatic repulsion. The latter two are particle chemistry dependent interparticle forces, with VDW dominating and increasing with decreasing particle size [38]. Yang et al. [38] simulated the trajectories of nanoparticles in a PBF-LB melt pool. They conclude that for separated nanoparticles in the melt, the melt-flow-driven effect dominates the motion of the nanoparticles, and that increased nanoparticle floating is observed with increasing nanoparticle size. This indicates that smaller particles are less affected by the melt-flow induced forces, while the VDW forces become more pronounced, which should counteract a break-up of nanoparticle agglomerates with decreasing particle and agglomerate size. Yuan et al. [13] performed simulations and experiments with TiC nanoparticles (50 nm) and AlSi10Mg matrix processed in PBF-LB and concluded that processing with sufficient energy densities can deagglomerate nanoparticle clusters. However, even if deagglomeration could in principle occur in the melt pool, the present study verifies that it is not happening for the vast majority of TiCnm agglomerates.

The reason why the nanoparticles, which are integrated in the agglomerates prior to PBF-LB, do not separate in the melt pool is because they form a strong bond during laser irradiation. As mentioned in the results section, this is mostly due to a sintering process initiated by the formation of sinter necks. However, for adequate sintering in such a short time period, very high temperatures, close to the melting temperature of TiC, are necessary. The melting temperature of TiC is 3140 °C [2]. The very low absorptivity of Al ($\approx$ 9 %) of the laser radiation at wavelengths of 1060–1080 nm is counteracting reaching these high temperatures [44,45]. However, the addition of Si and the occurrence of multi-scattering between the powder particles lead to an improvement of the absorptivity [45,46]. Leis et al. [47] measured an absorptivity of about 45 % for AlSi10Mg, which has a similar composition as the AlSi7Mg0.6 used in this work. Although these high temperatures are potentially possible with very high laser power, they are usually avoided because they would lead to unstable process conditions due to massive element evaporation, as they are above the boiling point of aluminum (2470 °C) and close to the boiling point of Si (3260 °C) [48].

More precisely, however, it is not the temperatures of the melt pool that are relevant for sintering, but those of the TiC. TiC has an absorptivity of more than 80 % which is significantly higher than that of the matrix [32]. TiC also has a lower heat capacity than Al [13]. At 300 K it is approximately 33 % lower. The lower heat capacity in combination with the higher absorptivity makes it reasonable to assume that TiC experiences a faster heating and a higher peak temperature compared to Al. These high temperatures apparently initiate a sintering process between the nanoparticles of an agglomerate to form an NPO particle.

Fig. 11 shows that the degree of sintering between different NPO particles can vary within the same specimen despite constant process parameters. The reason for this is that the effective temperature reached by the agglomerates during the process can vary depending on their position in the melt pool and the type of laser interaction. It can be assumed that an agglomerate positioned on the surface of the exposed powder bed and directly irradiated by the laser will heat up much faster than an agglomerate inside of the powder bed heated by a laser beam that has lost some of its intensity after multiple scatterings. It is also worth noting that the laser used has a Gaussian energy distribution. This means that agglomerates located in the center of the laser path are heated the most, while the energy input at the edge of the laser spot (i.e. away from the scan vector centerline laterally) is less pronounced. Nevertheless, the AlSi7Mg0.6 melts and incorporates the TiCnm agglomerates. During irradiation of the next (adjacent) track, the TiCnm agglomerates are already embedded in the highly reflective matrix and thus the high energy input required to induce severe TiC sintering is no longer possible, even if they now would be directly beneath the high-intensity laser spot center.

4.3. Nanoparticle chemistry and distribution after PBF-LB

Fig. 16 shows that the small (< 100 nm) Ti-rich particles in the microstructure are not TiC and thus, presumably, precipitates formed after TiCnm dissolution. Even though there is no indication for a melting or disintegration of the NPO TiC *micro*particles, the presence of Ti-rich precipitates is evidence that there must have been a transformation of individual TiC *nano*particles (or very small TiCnm agglomerates) during PBF-LB.

The Ti-rich precipitates are likely to be Al_3Ti or $(Al_{1-x},Si_x)_3Ti$ as suggested by Mohanty et al. [39]. Himmler et al. [49] detected Si-rich regions when investigating the phase stability of Al_3Ti in AlSi alloys and Yang et al. [50] detected an Al replacement of 9–11 at.% by Si in the Al_3Ti particles. Supported by Fig. 14 and Fig. 16, it seems likely that Si may be incorporated into Al_3Ti precipitates also in the present material. To form these precipitates, either melting or dissolution of individual TiCnm must have happened during the PBF-LB.

Dissolution of TiC in liquid Al is known to be possible well below the melting temperature of TiC. Casting experiments have shown that TiC decomposes in liquid AlSi7 alloy at intermediate temperatures of 750 °C within 30 min [39]. In contrast to the behavior at low temperatures, TiC is thermodynamically stable in liquid Al at high temperatures [30]. Various values for the temperature threshold are reported in the literature. The simulation results of Kaverinsky et al. [29] indicate an exothermic TiC synthesis reaction in a Ti-C-Al system above about 700 °C. The equilibrium isothermal section of the ternary phase diagram of Ti–C–Al at 900 °C shows a stable two-phase region of TiC and Al as long as the Ti:C ratio is 1:1; which is the case when both elements are introduced into the system in the form of TiC particles [29]. In the casting experiments of Kennedy et al. [51], TiC appeared to be stable in liquid, commercially pure Al above 900 °C, but began to dissolve at lower temperatures. The authors suggest that the dissolution of TiC is a diffusion-controlled process. Mohanty et al. [39] verified the decomposition of TiC in AlSi alloy leaving behind a $(Al_{1-x},Si_x)_3Ti$ compound. They suggested that the decomposition of TiC in liquid Al is favored by additional Si. These authors worked with larger TiC particles (5–10 μm), lower melt temperatures of about 750 °C and much longer liquid lifetimes of about 30 min as compared to the present work. Therefore, the applicability of the results to the PBF-LB situation may be limited. Nevertheless, it is clear that even though TiC is stable at high temperatures, during solidification, at least for a very short time, the system must cross the critical temperature range where TiC is thermodynamically unstable, and the temperature is high enough to allow the diffusion-controlled dissolution process to occur.

If TiC dissolution is happening, it is obviously much less pronounced in our experiments than in conventional casting. The dimensions of the NPO TiC microparticles presented here are below the size range of the TiC particles used in the investigations of Mohanty et al. [39]. However, even under these circumstances, which would be favorable for dissolution, much of the TiC remains in the microstructure, as evidenced by the

detection of C together with Ti. This carbon would not be expected in $(Al_{1-x},Si_x)_3Ti$ and can be clearly attributed to NPO TiC microparticles. A mitigated dissolution in PBF-LB seems reasonable if the dissolution process is diffusion controlled, since the rapid solidification occurring in PBF-LB does not allow sufficient time for it.

The explained dissolution behavior is particularly relevant for *nano*particles, which could explain why the NPO *micro*particles remain as TiC. Smaller particles should have an increased tendency to dissolve because i) there is less material to transform and ii) the interface (as the relevant reaction area for diffusion-controlled processes) is larger per unit volume. In addition, the high surface energy present in small particles destabilizes them thermodynamically. This is consistent with the results of Chang et al. [52], who detected a size dependent reactivity of SiC particles with Al to form Al_4SiC_4 in PBF-LB. The smaller the SiC particles, they find, the higher the reactivity.

However, a size dependence would also fit to TiC disintegration based on a melting mechanism. A size-dependent melting point of nanoparticles is scientifically well established [53]. The melting point of nanoparticles is lower than that of the corresponding bulk materials and decreases as the nanoparticles become smaller [54]. Even if NPO TiC microparticles originally consisted of nanoparticles, most of them underwent significant sintering during laser irradiation, which gives them the character of microparticles rather than nanoparticles.

In the present study, we cannot conclusively decide if the process leading to the disintegration of TiCnm in PBF-LB is based on melting or dissolution. Both routes are more pronounced for individual nanoparticles rather than the NPO TiC microparticles. However, we consider the melting mechanism as more likely because of the high absorptivity of TiC and the reduced melting point of nanoparticles, as well as the limited time available for the diffusion-controlled dissolution mechanism, which additionally occurs at much lower temperatures and hence with slower disintegration rates.

4.4. Evaluation of grain refinement mechanisms

The ability of TiC to refine the microstructure of Al-based alloys in PBF-LB has been reported in the literature [18,43]. However, there is no detailed and satisfactory understanding of the root causes. Simple explanations are not able to explain the spatially varying degree of grain refinement on the length scale of a melt pool, i.e. why it is more pronounced at the melt pool boundaries. Hence, to understand the microstructure in the present study, a more detailed discussion including the prevalent undercooling is needed and the impact of the newly formed Ti-rich precipitates needs to be evaluated and compared to the effect of TiC.

TiC is known to be an efficient grain refiner in common aluminum-based casting alloys [55]. Cicco et al. [16] measured a significant decrease in the amount of undercooling that is necessary to trigger heterogeneous nucleation when TiC nanoparticles (30–50 nm) were added to the Al–Si casting alloy A356 (approx. 7 % Si). Heterogeneous nucleation can be intensified by increasing the amount of inoculants. The higher their volume fraction, the lower the undercooling required to activate the particles as nucleation site [56]. Fig. 10 shows that the intensity of grain refinement in the melt pool centers increases with TiCnm addition, being most pronounced for the 5 wt.% TiCnm composite. According to the deterministic model of Greer et al. [57], the undercooling required to activate a particle as a nucleant depends on its size. Larger particles initiate nucleation earlier, i.e., already at lower undercooling, while smaller particles will only become nucleants later. In our experiments, which include particles of different sizes, the higher the undercooling, the more TiC particles will become potential nucleants, resulting in a finer microstructure. Under classical casting conditions for aluminum alloys, the supercooling is significantly lower than the high constitutional and thermal supercooling present in PBF-LB, which is a result of the high cooling and solidification rates in this additive manufacturing technique. As a result, nanoparticles can also initiate grain refinement in PBF-LB, whereas in casting the critical particle

radius that must be exceeded is in the micrometer size range, making nanoparticles ineffective as nucleating agent [58].

He et al. [59] performed simulations for a PBF-LB melt pool of a steel and revealed the highest undercooling in the center at the top of the melt pool, leading to the expectation that the highest grain refinement efficiency should be at this location, assuming that the TiC particles act as nucleants and are homogeneously distributed in the melt pool. This is supported by Durga et al. [60] who performed PBF-LB experiments with ferritic stainless steel and TiN nanoparticle inoculants. Samy et al. [56] carried out simulations based on these experiments. The small TiN particles are ineffective nucleants at the melt pool boundaries due to low undercooling, but effective in the center of the melt pool due to the low thermal gradient G and the high solidification velocity R that prevails there. This results in higher undercoolings that are sufficient to activate the TiN as nucleants. The resulting microstructure offers a coarser and columnar grain structure at the melt pool boundaries and a fine equiaxed grain structure in the melt pool center. This is, however, exactly the opposite of what is observed in the present study, where we find the smallest grains at the melt pool boundaries. This indicates that either the TiC particles are not homogeneously distributed or that they are not the dominant nucleation sites.

According to our results, many of the individual TiCnm particles were dissolved during the PBF-LB process, forming Al_3Ti precipitates (see previous section). Even if TiC is, from a crystallographic point of view, an effective heterogeneous nucleant for an Al matrix, Al_3Ti should be even more effective [16,25]. Although NPO TiC microparticles could act as heterogeneous nucleants, the number density of Ti-rich precipitates is much higher, indicating that if the precipitates are Al_3Ti and can therefore act as nucleation sites, they should dominate grain refinement instead of residual TiC particles.

The fact that precipitates act as nucleation sites explains the higher grain refinement at the melt pool boundaries. Fig. 15 verifies that the Al3Ti precipitates are almost absent in the melt pool center. This is known, for example, in Sc-containing, Al-based, PBF-LB fabricated parts where primary Al_3Sc is formed in larger size at the melt pool boundaries [61]. Opprecht et al. [27] also found a higher grain refinement in a Zr-containing Al alloy at the melt pool boundaries. In their study, the Al_3Zr precipitates formed during solidification acted as heterogeneous nucleation sites. The highest density of primary Al_3Zr precipitates was found at the melt pool boundaries due to the slow solidification rate at this location. Consequently, the precipitate number density decreased toward the center of the melt pool as the solidification rate increased. At a certain point toward the melt pool center, the solidification velocity became so fast that the precipitation of Al_3Zr couldn't take place anymore, and Zr was trapped in solid solution. This resulted in elongated instead of equiaxed grains in the center of the melt pools. A difference in Al_3Ti number density between the melt pool boundaries and the center could be verified in the present study (see Fig. 15). In combination with the fact of smaller grains present at melt pool boundaries, we assume that heterogeneous nucleation by Al-Ti-precipitates is the dominating mechanism of grain refinement in the material system discussed.

A broader equiaxed band at the melt pool boundaries can be linked to a higher number of nucleation sites, which reduce the necessary undercooling required for an equiaxed microstructure [56]. Following a similar reasoning, we conclude that our composite material made from the longer mixed powder blend contains a higher number of individual TiCnm and therefore a higher number of Al_3Ti precipitates during solidification (see Fig. 10), which, in turn, leads to a more pronounced grain refinement. The fact that the melt pool center regions also exhibit a refined and equiaxed grain structure indicates that heterogeneous nucleation is not restricted to the melt pool boundaries. Fig. 15 indicates that also above the fine-grained band a few Al_3Ti are present This may change at some point as you move further away from the melt pool boundary towards the center. But even if Al-Ti precipitation were entirely inhibited in the melt pool center, NPO TiC microparticles could still act as nucleants in these locations.

5. Conclusion

This work demonstrated that it is possible to fabricate TiC nanoparticle reinforced aluminum matrix composites (AMCs) via PBF-LB by using powder blends as feedstock material. As an economical and easily available approach, this procedure can be recommended especially for low nanoparticle contents. The blending duration and the laser exposure are crucial elements which define the final microstructure. The following conclusions can be drawn:

- Densified big TiC nanoparticle agglomerates are forming in the initial steps of the blending process.
- A long mixing duration is necessary to break up the big TiC nanoparticle agglomerates and to distribute the TiC nanoparticles on the surface of the AlSi7Mg0.6 particles, partly separated and partly in form of particle shell agglomerates.
- Since big agglomerates are pushed over the baseplate into the collector, less TiC remains in the final composite. This effect is more pronounced the more big TiC nanoparticle agglomerates there are in the feedstock powder.
- TiC nanoparticle agglomerates which undergo laser exposure show severe sintering between the particles making the corresponding TiC nanoparticles lose their nanoparticulate character.
- Unagglomerated TiC nanoparticles disintegrate, probably due to a melting process, and Ti-rich precipitates, likely $(Al,Si)_3Ti$, form during cooling after laser melting.
- Formation of $(Al,Si)_3Ti$ is more pronounced at the melt pool boundaries due to a slower solidification velocity, leading to a fine-grained zone due to heterogeneous nucleation.
- Nanoparticle-originating TiC microparticles in the melt pool center lead to a grain refinement in the melt pool center, but this is less pronounced compared to the grain refinement at the melt pool boundaries.
- A homogeneous equiaxed fully grain refined grain structure can be achieved by a high TiC nanoparticle content of 5 wt.% added to the AlSi7Mg0.6 matrix powder.

Further investigations must be conducted to verify the crystal structure and exact composition of the Ti-rich precipitates. In addition, the limit for TiC nanoparticle content must be evaluated and limiting factors assessed. Furthermore, the impact of the TiC addition on the mechanical properties including strength and ductility must be examined to check the potential of this material for future applications.

CRediT authorship contribution statement

Raphael Freundl: Writing – original draft, Visualization, Validation, Methodology, Investigation, Formal analysis, Data curation. **Eric A. Jägle:** Writing – review & editing, Supervision, Resources, Project administration, Conceptualization.

Declaration of competing interest

The authors declare that they have no known competing financial interests or personal relationships that could have appeared to influence the work reported in this paper.

Acknowledgement

Appendix

Table 1
Inspection certificate values for the elemental composition of the AlSi7Mg0.6 powder.

Element	Al	Si	Mg	Fe	Cu	Zn	Ti	Mn
Norm val. [%]	bal.	6.50-7.50	0.45-0.70	≤ 0.20	≤ 0.05	≤ 0.07	0.08-0.25	≤ 0.10
Actual val. [%]	bal.	6.60	0.58	0.15	0.001	< 0.005	0.2	0.006

Table 2
Inspection certificate values for the size distribution of the AlSi7Mg0.6 powder.

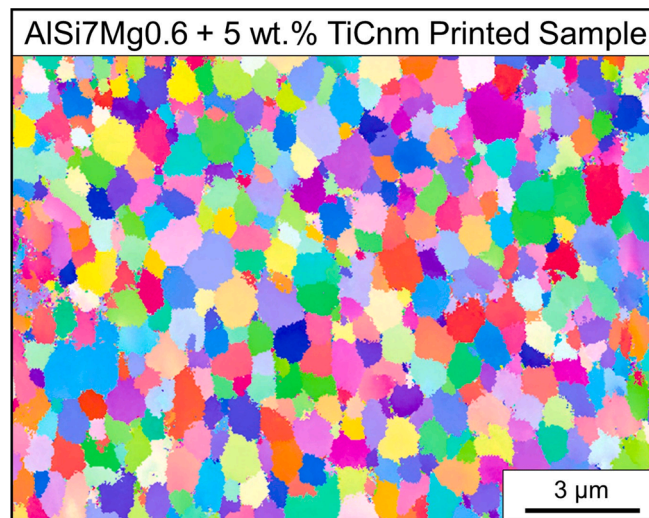| Size	D10	D50	D90
Actual val. [μm]	26.07	42.23	62.14

Fig. 17. Grain structure of the composite made from the blend with 5 wt.% TiCnm.

Data availability

Data will be made available on request.

References

[1] A. Mortensen, J. Llorca, Annu. Rev. Mater. Res. 40 (2010) 243–270.

[2] K.U. Kainer, Metal matrix composites: Custom-made materials for automotive and aerospace engineering, Wiley-VCH, Weinheim, Chichester, 2006.

[3] N. Behm, H. Yang, J. Shen, K. Ma, L.J. Kecskes, E.J. Lavernia, J.M. Schoenung, et al., Mater. Sci. Eng. A 650 (2016) 305–316.

[4] A.R. Bhardwaj, A.M. Vaidya, P.D. Meshram, D. Bandhu, Int. J. Interact. Des. Manuf. 18 (2024) 2911–2925.

[5] R. Bertolini, G. Andrea, N. Tamil Alagan, S. Bruschi, Wear 523 (2023), 204785.

[6] J. Kim, L. Zani, A. Abdul-Kadir, L. Jones, A. Roy, L. Zhao, V.V. Silberschmidt, Manuf. Lett. 32 (2022) 63–66.

[7] K.K. Sadhu, N. Mandal, R.R. Sahoo, J. Manuf. Process. 91 (2023) 10–43.

[8] N. Chawla, K.K. Chawla, Metal matrix composites, 2nd ed., Springer, New York [U. A.], 2013.

[9] D.G. Thomas, J. Colloid Sci. 20 (1965) 267–277.

[10] H.A. Barnes, J.F. Hutton, K. Walters, H.A. Barnes (Eds.), An Introduction to Rheology, Elsevier, Amsterdam, 1989.

[11] J. Jue, D. Gu, K. Chang, D. Dai, Powder Technol. 310 (2017) 80–91.

[12] M.B. Wilms, S.-K. Rittinghaus, M. Goßling, B. Gökce, Prog. Mater Sci. 133 (2023) 101049.

[13] P. Yuan, D. Gu, D. Dai, Mater. Des. 82 (2015) 46–55.

[14] D. Gu, P. Yuan, J. Appl. Phys. 118 (2015) 233109.

[15] G. Wang, Y. Zhang, B. Zou, Y. Liu, S. Zheng, X. Li, W. Yan, et al., Int. J. Plast 164 (2023) 103591.

[16] M.P. de Cicco, L.-S. Turng, X. Li, J.H. Perepezko, Metall and Mat Trans A 42 (2011) 2323–2330.

[17] F.H. Tong X.C.,, Metall. Mater. Trans. A 29 (1998) 893–902.

[18] T.-C. Lin, C. Cao, M. Sokoluk, L. Jiang, X. Wang, J.M. Schoenung, E.J. Lavernia, et al., Nat. Commun. 10 (2019) 4124.

[19] X.P. Li, G. Ji, Z. Chen, A. Addad, Y. Wu, H.W. Wang, J. Vleugels, et al., Acta Mater. 129 (2017) 183–193.

[20] L. Poovazhagan, K. Kalaichelvan, T. Sornakumar, Mater. Manuf. Process. 31 (2016) 1275–1285.

[21] S.A. Sajjadi, H.R. Ezatpour, M. Torabi Parizi, Mater. Des. 34 (2012) 106–111.

[22] M. Karbalaei Akbari, H.R. Baharvandi, K. Shirvanimoghaddam, Mater. Des. (1980–2015) 66 (2015) 150–161.

[23] K.R. Padmavathi, R. Ramakrishnan, L. Karthikeyan, S. Tamizhselvan, S. Chezhian Babu, Mater. Today: Proc. 72 (2023) 1996–2001.

[24] P.S. Mohanty, J.E. Gruzleski, Acta Metall. Mater. 43 (1995) 2001–2012.

[25] M. Zhang, P. Kelly, M. Easton, J. Taylor, Acta Mater. 53 (2005) 1427–1438.

[26] P. Mair, V.S. Goettgens, T. Rainer, N. Weinberger, I. Letofsky-Papst, S. Mitsche, G. Leichtfried, J. Alloy. Compd. 863 (2021) 158714.

[27] M. Opprecht, J.-P. Garandet, G. Roux, C. Flament, M. Soulier, Acta Mater. 197 (2020) 40–53.

[28] B. Ilschner, R.F. Singer, Werkstoffwissenschaften und Fertigungstechnik, Springer, Berlin Heidelberg, Berlin, Heidelberg, 2016.

[29] V.V. Kaverinsky, G.A. Bagliuk, Z.P. Sukhenko, J. Mater. Eng. Perform (2023).

[30] A. Albiter, A. Contreras, E. Bedolla, R. Perez, Compos. A Appl. Sci. Manuf. 34 (2003) 17–24.

[31] Y. Li, D. Gu, Mater. Des. 63 (2014) 856–867.

[32] N.K. Tolochko, Y.V. Khlopkov, S.E. Mozzharov, M.B. Ignatiev, T. Laoui, V.I. Titov, Rapid Prototyp. J. 6 (2000) 155–160.

[33] S.D. Jadhav, P.P. Dhekne, E. Brodu, B. van Hooreweder, S. Dadbakhsh, J.-P. Kruth, J. van Humbeeck, et al., Mater. Des. 198 (2021) 109369.

[34] G. Xue, L. Ke, H. Liao, C. Chen, H. Zhu, J. Alloy. Compd. 845 (2020) 156260.

[35] M. Wang, B. Song, Q. Wei, Y. Shi, J. Alloy. Compd. 810 (2019) 151926.

[36] W. Zhai, W. Zhou, S.M.L. Nai, J. Wei, J. Mater. Sci. Technol. 47 (2020) 162–168.

[37] E. Gärtner, H.Y. Jung, N.J. Peter, G. Dehm, E.A. Jägle, V. Uhlenwinkel, L. Mädler, Powder Technol. 379 (2021) 585–595.

[38] Y. Yang, C. Doñate-Buendía, T.D. Oyedeji, B. Gökce, B.-X. Xu, Materials (Basel, Switzerland) 14 (2021).

[39] P.S. Mohanty, J.E. Gruzleski, Acta Mater. 44 (1996) 3749–3760.

[40] D. Gu, H. Wang, F. Chang, D. Dai, P. Yuan, Y.-C. Hagedorn, W. Meiners, Phys. Procedia 56 (2014) 108–116.

[41] D. Gu, H. Wang, D. Dai, F. Chang, W. Meiners, Y.-C. Hagedorn, K. Wissenbach, et al., J. Laser Appl. 27 (2015) S17003.

[42] D. Gu, H. Wang, D. Dai, P. Yuan, W. Meiners, R. Poprawe, Scr. Mater. 96 (2015) 25–28.

[43] L. Xinwei, S. Shi, H. Shuang, H. Xiaogang, Z. Qiang, L. Hongxing, L. Wenwu, et al., Addit. Manuf. 34 (2020) 101326.

[44] E. Louvis, P. Fox, C.J. Sutcliffe, J. Mater. Process. Technol. 211 (2011) 275–284.

[45] A. Ghasemi, E. Fereiduni, M. Balbaa, S.D. Jadhav, M. Elbestawi, S. Habibi, Addit. Manuf. 46 (2021) 102145.

[46] C.D. Boley, S.C. Mitchell, A.M. Rubenchik, S.S.Q. Wu, Appl. Opt. 55 (2016) 6496–6500.

[47] A. Leis, R. Weber, T. Graf, Procedia CIRP 94 (2020) 173–176.

[48] Y. Zhang, J.R.G. Evans, S. Yang, J. Chem. Eng. Data 56 (2011) 328–337.

[49] D. Himmler, P. Randelzhofer, C. Körner, Results in Materials 7 (2020) 100103.

[50] C. Yang, Z. Liu, Q. Zheng, Y. Cao, X. Dai, L. Sun, J. Zhao, et al., J. Alloy. Compd. 747 (2018) 580–590.

[51] A.R. Kennedy, D.P. Weston, M.I. Jones, Mater. Sci. Eng. A 316 (2001) 32–38.

[52] F. Chang, D. Gu, D. Dai, P. Yuan, Surf. Coat. Technol. 272 (2015) 15–24.

[53] K.K. Nanda, Pramana - J Phys 72 (2009) 617–628.

[54] W.H. Qi, M.P. Wang, Mater. Chem. Phys. 88 (2004) 280–284.

[55] G.S. Vinod Kumar, B.S. Murty, M. Chakraborty, J. Alloy. Compd. 396 (2005) 143–150.

[56] V.P. Narayana Samy, M. Schäfle, F. Brasche, U. Krupp, C. Haase, Addit. Manuf. 73 (2023) 1–14.

[57] A. Greer, A. Bunn, A. Tronche, P. Evans, D. Bristow, Acta Mater. 48 (2000) 2823–2835.

[58] P. Mair, L. Kaserer, J. Braun, N. Weinberger, I. Letofsky-Papst, G. Leichtfried, Mater. Sci. Eng. A 799 (2021) 140209.

[59] Y. He, M. Zhong, N. Jones, J. Beuth, B. Webler, Metall Mater Trans A 52 (2021) 4206–4221.

[60] A. Durga, N.H. Pettersson, S.B.A. Malladi, Z. Chen, S. Guo, L. Nyborg, G. Lindwall, Scr. Mater. 194 (2021) 113690.

[61] Q. Jia, P. Rometsch, P. Kürnsteiner, Q. Chao, A. Huang, M. Weyland, L. Bourgeois, et al., Acta Mater. 171 (2019) 108–118.